Journal of Nuclear Materials 378 (2008) 60–69

Contents lists available at ScienceDirect

Journal of Nuclear Materials

journal homepage: www.elsevier.com/locate/jnucmat

A model to describe the anisotropic viscoplastic mechanical behavior of fresh and irradiated Zircaloy-4 fuel claddings under RIA loading conditions

M. Le Saux [a,b,*], J. Besson [b], S. Carassou [a], C. Poussard [a], X. Averty [a]

[a] CEA-Saclay, DEN/DMN/SEMI, 91191 Gif-Sur-Yvette, France
[b] Centre des Matériaux, Mines Paris, CNRS UMR 7633, 91003 Evry, France

ARTICLE INFO

Article history:
Received 28 January 2008
Accepted 25 April 2008

PACS:
62.20.−x
62.20.Fe

ABSTRACT

This paper presents a unified phenomenological model to describe the anisotropic viscoplastic mechanical behavior of cold-worked stress relieved (CWSR) Zircaloy-4 fuel claddings submitted to reactivity initiated accident (RIA) loading conditions. The model relies on a multiplicative viscoplastic formulation and reproduces strain hardening, strain rate sensitivity and plastic anisotropy of the material. It includes temperature, fluence and irradiation conditions dependences within RIA typical ranges. Model parameters have been tuned using axial tensile, hoop tensile and closed-end internal pressurization tests results essentially obtained from the PROMETRA program, dedicated to the study of zirconium alloys under RIA loading conditions. Once calibrated, the model provides a reliable description of the mechanical behavior of the fresh and irradiated (fluence up to 10×10^{25} nm^{-2} or burnup up to 64 GWd/tU) material within large temperature (from 20 °C up to 1100 °C) and strain rate ranges (from 3×10^{-4} s^{-1} up to 5 s^{-1}), representative of the RIA spectrum. Finally, the model is used for the finite element analysis of the hoop tensile tests performed within the PROMETRA program.

1. Introduction

The need to increase fuel burnup in pressurized water reactors (PWR) initiated safety studies aiming at evaluating the consequences of postulated events on higher burnup fuels. Reactivity initiated accidents (RIA), for which the postulated initiator is the inadvertent ejection of a control rod, are among the most severe design basis accidents. This accident generates a fast energy injection in the fuel (about 50 ms), leading to a rapid expansion of the fuel pellets (with thermal and possibly fission gases contributions). The surrounding cladding tube is then submitted to pellet-clad mechanical interaction (PCMI), which results in a strain-controlled multiaxial mechanical loading under high strain rate (typically 1 s^{-1}) associated with a high heating rate (about 10^3 °C/s) thermal loading. Since the clad remains at fairly low temperatures during this early stage of the transient (below 800 °C if starting from hot zero power conditions), the fast mechanical loading generated may cause partially brittle failures of high burnup fuel claddings, embrittled due to metal–water reactions and accumulation of irradiation damage during reactor exposure. At a later stage of the transient, a departure of nucleate boiling (DNB) may occur at the clad outer surface due to the heat transferred from the pellets. Then, the cladding material could remain at high temperatures (above 800 °C) for several seconds, until rewetting. During this fairly long period, rod internal pressure may increase, due to fission gas release after pellet-clad gap re-opening, and lead to clad failure through pressure-controlled clad ballooning. The evaluation of the risk of rod failure during RIAs currently requires the use of transient fuel behavior codes [1]. These codes are developed in conjunction with full-scale experiments [2], in order to provide an accurate interpretation of the tests with the aim of transposing results to the reactor case.

For that purpose, suitable models are necessary to describe the mechanical behavior of fuel claddings under RIA conditions. Several models, either based on macroscopic constitutive equations [3–5] or micromechanical polycrystalline descriptions [6–8], have been proposed in the literature to simulate the mechanical behavior of zirconium alloys cladding materials. However, most of them are not appropriate in the field of RIA studies as they are usually restricted to limited temperature and strain rate ranges specific of normal or slightly off-normal conditions. Moreover, micromechanical models still remain too complex and CPU-time consuming to be used in transient fuel behavior codes, although efforts have been made to avoid these restrictions [7]. Within this framework, the present paper proposes a macroscopic constitutive model to describe the anisotropic viscoplastic behavior of fresh and highly irradiated cold-worked stress relieved (CWSR) Zircaloy-4 fuel

* Corresponding author. Address: CEA-Saclay, DEN/DMN/SEMI, 91191 Gif-Sur-Yvette, France. Tel.: +33 1 69 08 18 18; fax: +33 1 69 08 93 24.
E-mail address: matthieu.lesaux@cea.fr (M. Le Saux).

0022-3115/$ - see front matter © 2008 Elsevier B.V. All rights reserved.
doi:10.1016/j.jnucmat.2008.04.017

claddings under RIA loading conditions. Suitable out-of-pile tests results, essentially collected from the PROMETRA (TRAnsient MEchanical PROperties) program [9–12], carried out in Commissariat à l'Energie Atomique (CEA) hot laboratories and undertaken by the French Institut de Radioprotection et de Sûreté Nucléaire (IRSN) in collaboration with Electricité de France (EdF) and CEA, have been gathered for the identification of the model parameters within temperature and strain rate ranges representative of those encountered during RIA transients.

This paper is organized as follows. The material under study and the selected experimental database are described in Section 2. The anisotropic viscoplastic mechanical properties of the material are then discussed. In particular, the influences of test temperature, strain rate, fluence and irradiation conditions are analyzed. In Section 3, the formulation of the proposed model is detailed and its ability to reproduce, once calibrated, the experimental data is illustrated. Finally, using the present model to describe the mechanical behavior of the cladding specimens, a Finite Element Analysis (FEA) of the hoop tensile tests performed within the PROMETRA program is presented in Section 4.

2. Experimental observations

2.1. Material and experimental database

The material consists in CWSR Zircaloy-4 tubes, which is commonly used for fuel claddings in PWRs. Its weight composition is 1.2–1.7% Sn, 0.18–0.24% Fe, 0.07–0.13% Cr, 0.1–0.14% O, Zr balance, according to the ASTM B 350.90 specification. Before irradiation, the cladding tubes present a nominal external diameter and a thickness of 9.5 mm and 0.57 mm, respectively. The stress relieved state is obtained by heat treatment at a temperature lower than 500 °C. The grains then remain elongated along the rolling direction (tubes axial direction) and the density of dislocations is high, resulting in a high mechanical strength. The fabrication process of cladding tubes leads to the development of a strongly marked crystallographic texture of the material (typically, the $\langle c \rangle$ directions are symmetrically oriented at about 30° from the tube radial direction in the radial-tangential plane).

The PROMETRA experimental database was used to study the mechanical behavior of the material under thermal–mechanical loading conditions representative of those generated during RIAs. This database gathers uniaxial axial tensile (AT) and hoop tensile (HT) tests and biaxial (axial to hoop stress ratio of 0.5) closed-end internal pressurization (IP) burst tests results for the non-irradiated and the irradiated material (fluence up to about 10×10^{25} nm^{-2} or burnup up to 64 GWd/tU). Geometries of the specimens tested within the PROMETRA program are detailed in Fig. 1. These tests were performed under high strain rate (from 0.01 s^{-1} to 5 s^{-1}) within a large temperature range (from 20 °C up to 1100 °C). The irradiated specimens were machined from fuel cladding tubes irradiated in French PWRs. Except for some IP samples, the oxide layer of irradiated tubes was beforehand mechanically removed. The tests were performed under constant temperature. A furnace heating technique (slow heating rate, about 0.2 °C/s) was used for the tests conducted below 480 °C. For higher temperatures, fast heating techniques, using the Joule effect (about 100 °C/s) for AT tests and an induction heating system (about 200 °C/s) for HT tests, were used to minimize the potential annealing, hydrides redistribution or even recrystallization of the material (which are highly time-dependent processes [10]). For AT and HT tests, engineering strain and engineering stress were respectively calculated by dividing the cross-head displacement by the specimen initial gauge length and the applied force by the initial cross-section. For IP tests, the mean engineering hoop strain

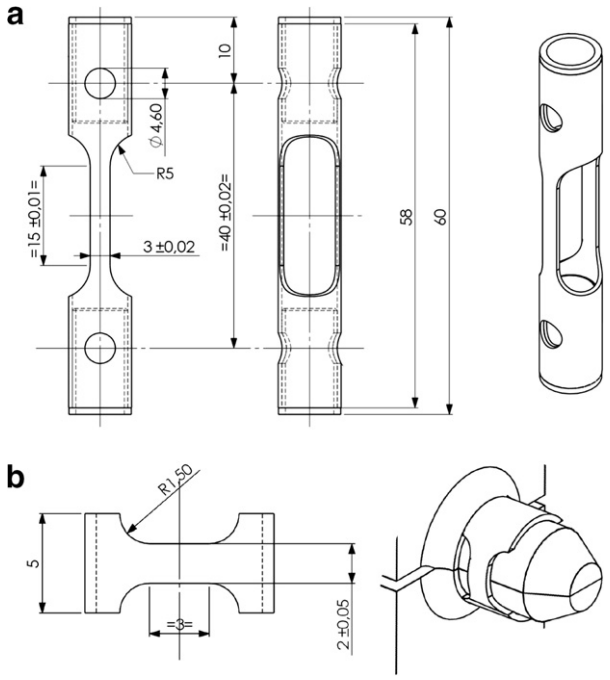

Fig. 1. (a) AT specimen and (b) HT specimen (mandrels used to load the specimen are shown on the right) tested within the PROMETRA program.

in the tube thickness is equal to $\Delta D_e/D_m$, where D_e and D_m are respectively the external and the initial mean tube diameter, and the difference between the engineering values of hoop and radial stresses is given by $PD_m/2t$, where P is the internal pressure and t is the initial tube thickness. In conformity with the negligible contribution during RIAs of elastic strains compared to plastic strains, the present paper only focuses on the inelastic behavior of the material. Parameters such as the yield stress at 0.2% plastic strain, $S_Y^{0.2\%}$, the ultimate (or maximum) stress, S_U, and the uniform elongation at the onset of necking (plastic strain which corresponds to S_U), e_U, were determined on the engineering stress–strain curves. True plastic strain and true stress are denoted ϵ^p and σ, respectively. Tests conducted on specimens machined in spalled areas of highly corroded claddings were not considered since hydride blisters, which significantly affect the macroscopic mechanical behavior of the material, are generally observed in those regions [12]. Moreover, the determination of hoop tensile stress–strain properties from HT tests performed on ring specimens is complex due to structural effects such as bending and friction. Nevertheless, as revealed by FEA of the HT tests performed within the PROMETRA program (described in Section 4), whereas the influence of these effects are significant within the elastic domain and at the onset of plasticity, one can assume that the ultimate stress is only slightly affected. Hence, for HT tests, only the ultimate stresses have been considered. Note that an international Round Robin, currently pursued, has been launched in 2001 in order to compare the results obtained from different methods involving various sample geometries and experimental devices [13,15,11,14] for generating hoop tensile properties [16].

Experimental results extracted from the open access [17,18] and restricted literature were also used in order to enlarge the experimental database, in particular for low temperatures (from 20 °C to 350 °C) and low strain rates (3×10^{-4} s^{-1}). Due to confidentiality reasons, some of these data will not explicitly appear in the figures shown in this paper. Finally, the experimental database gathers 521 tests results divided as listed in Table 1. These data reveal an evident scatter, especially for the irradiated

Table 1
Exploited experimental database

Tests	Fresh material		Irradiated material[a]	
	Ranges	Number	Ranges	Number
AT	20–1100 °C 3×10^{-4}–5 s^{-1}	54	20–1100 °C 3×10^{-4}–5 s^{-1}	124
HT	20–900 °C 3×10^{-4}–5 s^{-1}	34	20–600 °C 3×10^{-4}–5 s^{-1}	168
IP	20–400 °C 3×10^{-4}–1.5×10^{-2} s^{-1}	59	20–350 °C 3×10^{-4}–1.5×10^{-2} s^{-1}	82

[a] From 1 cycle up to 5 cycles in PWR.

material, due to the various origins of the material and to uncertainties on irradiation and testing conditions. Furthermore, evaluation of uniform elongation is difficult due to the low hardening properties of the material.

2.2. Analysis of the experimental data

Strength, strain hardening, strain rate sensitivity and plastic anisotropy of the material have been analyzed. Their dependence on temperature, fluence, irradiation conditions and plastic strain are discussed below.

2.2.1. Strength

For all testing conditions (AT, HT or IP tests), the flow stress of the fresh material normally decreases with increasing temperature, T, due to the increase of dislocations mobility (Fig. 2a). A slight inflection can be observed between about 300 °C and 600 °C.

Besides, comparison of Fig. 2a and b shows that neutron irradiation leads to a significant hardening (*i.e.* increase in flow stress) of the material, due to the formation of point defect clusters (high density of irradiation-induced loops) that act as obstacles against the glide of deformation dislocations [6,19,20]. This effect is significant at low fluences, ϕ_t ($E > 1$ MeV), then quickly saturates beyond about 2×10^{25} nm^{-2} (*i.e.* one annual cycle in PWR). The saturation is related to a balance between the creation and the recombination of irradiation defects. Amplitude of the irradiation hardening significantly decreases with increasing test temperature, in particular beyond the irradiation temperature (about 350 °C), due to a partial recovery of the out of equilibrium microstructure of the irradiated material (reduction of the point defects density and growth of the irradiation-induced loops). The flow stress of the irradiated material tends towards that of the non-irradiated material at high test temperatures, for which irradiation defects are quasi-instantaneously recovered according to literature results (see [21] for example).

Moreover, mechanical properties of the material depend on irradiation conditions. Irradiation temperature is not uniform along fuel cladding tubes (it varies from about 320 °C to 380 °C) since temperature of the primary coolant is higher at the upper part of the assembly. As the external oxide layer acts as a heat insulator, the thermal gradient along fuel claddings is intensified by the faster clad oxidation kinetics for the higher, warmer spans. Therefore, the irradiation hardening amplitude depends, in addition to fluence, on the original state of the tested specimen, depending on its axial position along the tubes. Fig. 3 shows in accordance with the observations reported in [22] that, for a same neutron fluence, the flow stress of the material decreases with increasing normalized axial position $\xi = z/l$, where z is the axial position computed from the bottom of the assembly and l is the total length

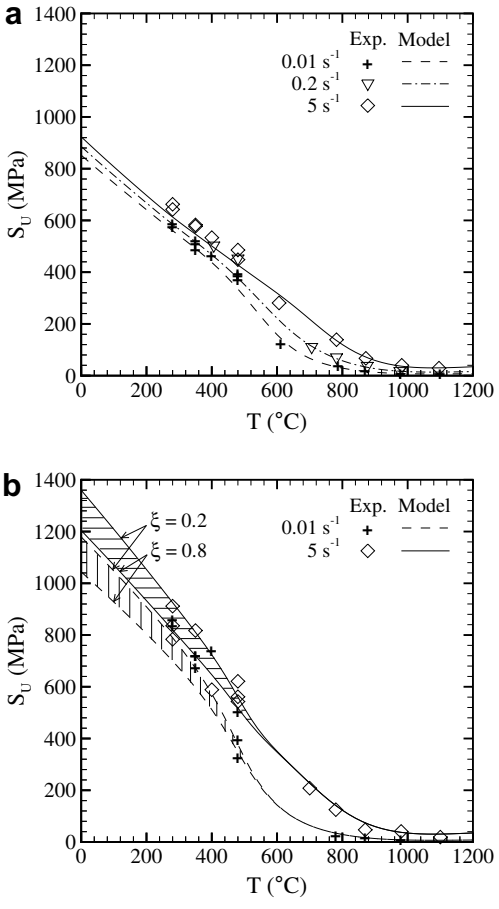

Fig. 2. Variation of the ultimate stress as a function of temperature and strain rate for AT tests performed (a) on the fresh material and (b) on the material irradiated for 5 cycles (fluence around 10×10^{25} nm^{-2}).

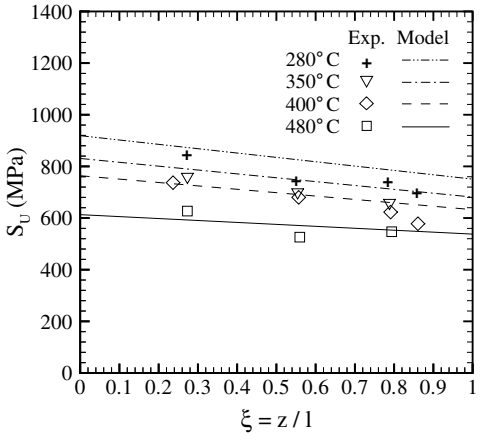

Fig. 3. Variation of the ultimate stress as a function of the normalized axial position of the specimen along the cladding tubes for HT tests conducted at various temperatures under a strain rate of 5 s^{-1} on the material irradiated for 5 cycles.

of the cladding tube (for example, $l = 3.66$ m for french PWR 900 MW reactors). Actually, a higher irradiation temperature allows a more efficient recombination of point defects and thus a lower density of loops after irradiation [19]. One can expect that the axial position effect (or more specifically the irradiation temperature effect) is attenuated with increasing test temperature, in particular above the irradiation temperature. Indeed, magnitude of the variation of material strength as a function of the axial position/irradiation temperature increases with increasing the irradiation time.

2.2.2. Strain hardening

As shown in Figs. 4 and 5, the instantaneous strain hardening exponent of the material,

$$n = \frac{\partial \ln \sigma}{\partial \ln \epsilon^p} = \frac{\epsilon^p}{\sigma}\frac{\partial \sigma}{\partial \epsilon^p}, \quad (1)$$

varies continuously during plastic deformation; it slightly increases with plastic strain at low plastic strain levels (less than 0.5%) and decreases at higher strain levels. The influence of plastic strain on the strain hardening behavior of Zircaloy-4 fuel claddings is often ignored by other investigators, who consider one average strain hardening exponent over a large plastic strain range. For example, an average strain hardening exponent of about 0.06 is reported in [23] for the fresh material at 300 °C. This value is in good agreement with the mean value, calculated up to uniform elongation, of the instantaneous strain hardening exponent depicted in Fig. 5. The instantaneous strain hardening globally decreases with increasing temperature, which is consistent with the thermally activated dislocation cross-slip and climb. Besides, it decreases with increasing irradiation, in particular for plastic strains close to the uniform elongation. Indeed, independently of plastic deformation, the flow stress σ increases with irradiation. Furthermore, according to Onimus et al. observations [6,24], the strain hardening rate $\partial\sigma/\partial\epsilon^p$ of the irradiated material is clearly higher at the onset of plastic flow (due to the plastic strain localization at the grain scale). Then, it rapidly decreases (channels propagation from grain to grain) to values of the same order of magnitude than for the non-irradiated material, that decreases more gradually. In accordance, the uniform strain continuously decreases with increasing temperature. Irradiation leads to a clear reduction in uniform elongation, associated to a highly localized necking, as previously observed by Regnard et al. [20]. The irradiation effect on the strain hardening behavior is reduced with increasing test temperature (irradiation damage recovery).

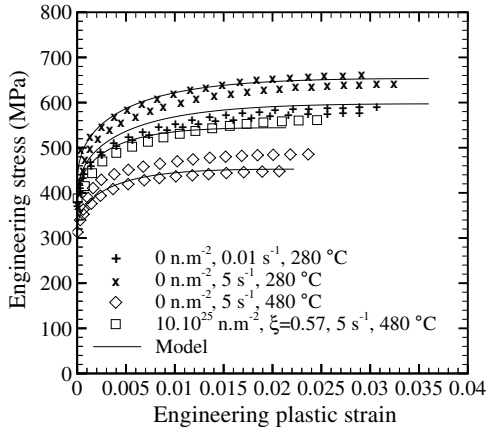

Fig. 4. Experimental (symbols) and simulated (lines) engineering stress–plastic strain curves (up to uniform elongation) for AT tests performed under various conditions on the non-irradiated material and the material irradiated for 5 cycles.

2.2.3. Strain rate sensitivity

Fig. 2 also illustrates the strain rate sensitive strength of the material. The strain rate sensitivity, defined as the change in flow stress over a strain rate range, is described by the parameter,

$$m = \frac{\partial \ln \sigma}{\partial \ln \dot{\epsilon}}, \quad (2)$$

which can be approximated by $m \approx (\ln \sigma_2 - \ln \sigma_1)/(\ln \dot{\epsilon}_2 - \ln \dot{\epsilon}_1)$ where σ_1 and σ_2 are the flow stresses measured during tests conducted – for similar test temperature, irradiation conditions and plastic strain level – under strain rates $\dot{\epsilon}_1$ and $\dot{\epsilon}_2$, respectively. As shown in Fig. 6, whatever the test temperature, the strain rate sensitivity is positive, *i.e.* the flow stress increases with increasing strain rate. It is nearly constant between 20 °C and 300 °C and increases significantly beyond. No evidence of drop in strain rate sensitivity, manifestation of dynamic strain aging (due to the mutual interaction between the oxygen solute atoms and the dislocations) sometimes observed around 350 °C (depending on strain rate) in zirconium alloys [25,18], is detected. Furthermore, as already observed in recrystallized zirconium alloys [24], it seems that

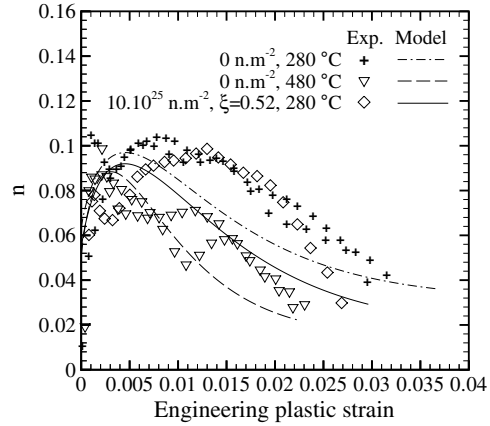

Fig. 5. Variation of the instantaneous strain hardening exponent, $n = \partial \ln \sigma / \partial \ln \epsilon^p$, as a function of plastic strain (up to uniform elongation) for AT tests performed under a strain rate of 5 s^{-1} on the non-irradiated material and the material irradiated for 5 cycles.

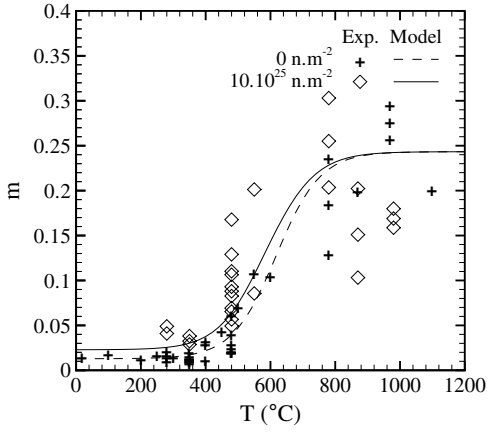

Fig. 6. Variation of the strain rate sensitivity exponent, $m = \partial \ln \sigma / \partial \ln \dot{\epsilon}$, as a function of temperature for AT tests performed on the non-irradiated material and the irradiated material for 5 cycles.

irradiation increases the strain rate sensitivity of the material for temperatures lower than about 500 °C.

2.2.4. Plastic anisotropy

Due to the hexagonal close-packed lattice of zirconium combined with the processing of fuel cladding tubes, the material exhibits a strong crystallographic texture implying anisotropic, and more specifically orthotropic mechanical properties in the tube reference system, defined by radial (r), hoop (θ) and axial (z) directions. For example, plastic anisotropy is highlighted by the ratios of axial to hoop plastic strain increments measured during AT and IP tests (Fig. 7) and by comparing the flow stresses measured during AT and HT tests (Figs. 2 and 9). The axial to hoop plastic strain ratios used in the present work are in good agreement with the approximate ratio of −1.8 reported in [3,4,15] for the non-irradiated material under axial tension at 350 °C. As shown in Fig. 7 and in accordance with the observations of Murty and Charit [26], plastic anisotropy of the fresh material depends on test temperature, in particular above 300 °C. Note that the variation as a function of temperature of plastic anisotropy is more marked for lower strain rates and plastic strain levels. This evolution may be partially explained by the activation of different slip systems depending on testing conditions. Whatever the test temperature and the plastic strain level, it has been established that prismatic glide is predominant for the non-irradiated material [27]. Nevertheless, other mechanisms are present: slip on the first pyramidal system has been observed at high plastic strains and high temperatures and, although hardly observed, basal glide becomes significant for high temperatures (above about 500 °C), low strain rates and high plastic strain levels. Moreover, as illustrated by the difference between flow stresses measured during AT and HT tests, plastic anisotropy of the material depends on irradiation. Note that studies dealing with the influence of irradiation on the plastic anisotropy of zirconium alloys are very few [28,30,29]. Onimus et al. [6,24] observed an irradiation-induced change in the principal slip system activation. Basal slip becomes the dominant deformation mechanism for the irradiated material, since the increase under irradiation of the critical resolved shear stresses for prismatic and pyramidal slip systems is greater than for the basal slip system. In addition, one can expect that hydrides generally observed in fuel claddings irradiated in PWRs may influence the material anisotropy.

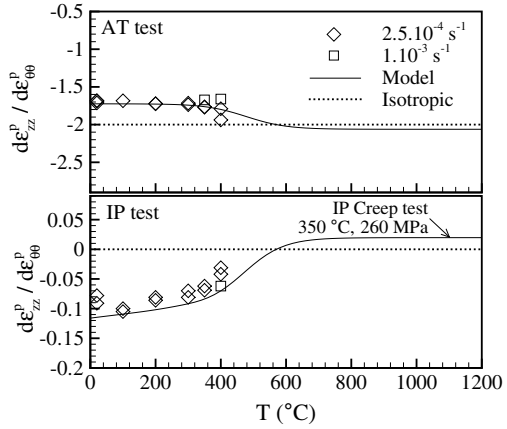

Fig. 7. Variations as a function of test temperature of the ratios of axial to hoop plastic strain increments obtained during AT tests (for axial plastic strain values of 0.01 and 0.02) and IP tests (for hoop plastic strain values of 0.01 and 0.015) conducted on the fresh material under various strain rates.

3. Model description

3.1. Model formulation

In order to reproduce these effects, a unified (only one type of inelastic deformation is considered) anisotropic viscoplastic model, with no stress threshold between elastic and viscoplastic regimes (and thus only appropriate for monotonic loading) and including a multiplicative plastic strain dependent strain hardening, is proposed. The total strain, $\underline{\epsilon}$, can be splitted up in an additive manner into elastic, $\underline{\epsilon}^{e}$, and viscoplastic, $\underline{\epsilon}^{p}$, parts. The elastic contribution, which is assumed to be isotropic, is described by a temperature dependent Young's modulus, $E(T)$, and a Poisson's ratio, ν, according to the isotropic Hooke's law.

The texture-induced plastic orthotropy of the material is described by a Hill's quadratic yield criterion [31] (isotropic hardening):

$$\sigma_{H}(\underline{\boldsymbol{\sigma}}, T, \phi_t) = \sqrt{\underline{\boldsymbol{\sigma}} : \underline{\underline{\mathbf{H}}}(T, \phi_t) : \underline{\boldsymbol{\sigma}}} \tag{3}$$

where $\underline{\boldsymbol{\sigma}}$ is the stress tensor and $\underline{\underline{\mathbf{H}}}$ is a symmetric fourth rank tensor. The equivalent stress has the following expression when expressed in the anisotropy principal axes, which coincide with the tube reference system axes (r, θ, z):

$$\sigma_{H} = [H_{rr}(\sigma_{\theta\theta} - \sigma_{zz})^2 + H_{\theta\theta}(\sigma_{zz} - \sigma_{rr})^2 + H_{zz}(\sigma_{rr} - \sigma_{\theta\theta})^2 + 2H_{r\theta}\sigma_{r\theta}^2 + 2H_{rz}\sigma_{rz}^2 + 2H_{\theta z}\sigma_{\theta z}^2]^{1/2}. \tag{4}$$

Since shear components are unknown and play no role in the simulated mechanical tests, they are assumed to be equal to the isotropic ones, *i.e.* $H_{r\theta} = H_{rz} = H_{\theta z} = 1.5$. In order to determine the anisotropy coefficients H_{rr}, $H_{\theta\theta}$ and H_{zz}, which are defined up to a multiplicative constant, the axial direction is fixed as the reference one, leading to $\sigma_{H} = \sigma_{zz}$ for an AT test so that $H_{rr} + H_{\theta\theta} = 1$ (normalization condition).

The viscoplastic strain rate tensor, $\underline{\dot{\epsilon}}^{p}$, obeys the normality rule and is expressed using a viscoplastic potential

$$\Omega = \dot{p}_0 \frac{m\eta}{m+1}\left(\frac{\sigma_{H}}{\eta}\right)^{\frac{1+m}{m}}, \tag{5}$$

so that

$$\underline{\dot{\epsilon}}^{p} = \frac{\partial \Omega}{\partial \underline{\boldsymbol{\sigma}}} = \dot{p}\frac{\partial \sigma_{H}}{\partial \underline{\boldsymbol{\sigma}}} = \dot{p}\underline{\underline{\mathbf{H}}} : \frac{\underline{\boldsymbol{\sigma}}}{\sigma_{H}}. \tag{6}$$

The equivalent viscoplastic strain rate is given by

$$\dot{p} = \dot{p}_0\left(\frac{\sigma_{H}(\underline{\boldsymbol{\sigma}}, T, \phi_t)}{\eta(p, T, \phi_t, \xi)}\right)^{1/m(T,\phi_t)}, \tag{7}$$

where m is the strain rate sensitivity exponent defined in Eq. (2), $\dot{p}_0$ is the reference strain rate fixed to 1 s^{-1} and η is a non-linear viscosity coefficient. For the sake of clarity, η is separated into strength and strain hardening contributions:

$$\eta(p, T, \phi_t, \xi) = K(T, \phi_t, \xi)L(p, T, \phi_t) \tag{8}$$

where K is the strength coefficient (independent on p) and L is the strain hardening coefficient (dependent on p). The strain hardening exponent of the material (Eq. (1)) is then given by $n = \partial \ln L / \partial \ln \epsilon^{p}$ under uniaxial loading.

3.2. Model identification

The proposed model includes four parameters to be adjusted: the strain rate sensitivity exponent m, the strength coefficient K, the strain hardening coefficient L and the Hill tensor $\underline{\underline{\mathbf{H}}}$. According to the experimental observations partially described in Section 2, m is considered as temperature and fluence dependent, K is defined

as temperature, fluence and irradiation conditions dependent, L is regarded as plastic strain, temperature and fluence dependent and $\underline{\underline{\mathbf{H}}}$ depends on temperature and fluence. Since the irradiation temperature is not available for the majority of the tested specimens, the influence of irradiation conditions is expressed in term of normalized axial position of the samples along the fuel cladding tubes, which is known for all the irradiated specimens. Nevertheless, an approximate linear relation between the irradiation temperature T_i and the normalized axial position ξ can be established from the few irradiation temperature data available: $T_i(\mathrm{K}) = 594.35 + 49.673\xi$.

Description of the strongly non-linear evolutions of these parameters as a function of plastic strain, temperature and fluence within wide ranges requires a large number of secondary parameters. The 46 resulting secondary parameters have been identified using the whole experimental database summarized in Table 1. The Newton's optimization method has been applied to minimize weighted least square cost functions introduced to characterize the difference between experimental data and model predictions. The general identification procedure is summarized in Table 2, where in particular the experimental data used to tune each parameter are specified.

Table 2
Identification procedure

Parameter	Signification	Data	Test
m	Strain rate sensitivity	$\sigma_Y^{x\%}$ [b]	AT
L	Strain hardening	$\sigma = f(\epsilon^p)$ up to ϵ_U if available	AT
		$\sigma_Y^{x\%}$ [b], σ_U and ϵ_U otherwise	AT
K	Strength	$\sigma_Y^{x\%}$ [b], σ_U	AT
$\underline{\underline{\mathbf{H}}}$	Anisotropy	$d\epsilon_{zz}^p/d\epsilon_{\theta\theta}^p$ [a]	AT
		σ_U	HT
		$d\epsilon_{zz}^p/d\epsilon_{\theta\theta}^p$ [a], $\sigma_Y^{x\%}$ [b] and σ_U	IP

[a] For the fresh material only.
[b] $x = 0.1, 0.2, 0.5, 1$ when available.

As a first step, while considering the normalization condition chosen for the determination of the Hill coefficients, the parameters m, L and K were evaluated using AT tests results. First, m and L were independently identified using for m: $\sigma_Y^{x\%}$ with $x = 0.1, 0.2, 0.5, 1$ when available; for L: $\sigma = f(\epsilon^p)$ up to ϵ_U if available, $\sigma_Y^{x\%}$ with $x = 0.1, 0.2, 0.5, 1$, σ_U and ϵ_U otherwise. Then, considering these adjusted values as the initial ones for the identification process, K was tuned on the basis of $\sigma_Y^{x\%}$ with $x = 0.1, 0.2, 0.5, 1$ and σ_U. A global adjustment of m, L and K was subsequently performed on all AT tests data.

Afterwards, parameters describing plastic anisotropy ($\underline{\underline{\mathbf{H}}}$) were identified on the basis of AT ($d\epsilon_{zz}^p/d\epsilon_{\theta\theta}^p$ available for the fresh material only), HT (σ_U) and IP ($d\epsilon_{zz}^p/d\epsilon_{\theta\theta}^p$ available for the fresh material only, $\sigma_Y^{x\%}$ with $x = 0.1, 0.2, 0.5, 1$ and σ_U) tests results. Note that for temperatures greater than 400 °C, only stress–plastic strain data in the hoop direction were available (up to 900 °C for the fresh material and 600 °C for the irradiated material) for the determination of anisotropy coefficients. However, since for a given loading direction the activated deformation mechanisms and consequently the macroscopic plastic anisotropy essentially depend on the local stress level, one can expect that anisotropy of the material subjected to high temperature and high strain rate strain hardening tests is closed to that deduced from creep tests conducted at moderated stress levels (low strain rate) under moderated temperatures. Hence, the anisotropy coefficients have also been identified so that the ratio $d\epsilon_{zz}^p/d\epsilon_{\theta\theta}^p$ predicted for IP tests tends, when increasing temperature, towards the ratio value of 0.019 deduced from IP creep tests conducted at 350 °C at a fixed stress level equal to 260 MPa up to a hoop plastic strain of 0.025 [17].

Finally, a global parameters adjustment was achieved over the whole experimental database. In order to avoid non-physical extreme parameter values and prevent numerical problems in simulation codes, all functions introduced to describe evolutions of model parameters have been defined so that smooth evolutions with lower and upper values are obtained. Tuned values of the parameters are reported in Table 3.

Table 3
Adjusted model parameters (T in K, ϕ_t in 10^{25} nm^{-2} and ξ in m/m)

Elasticity
$E(T) = 1.059 \times 10^{11} - 36 \times 10^6 T$, $\nu = 0.342$

Irradiation damage
$\Phi(\phi_t) = 1 - \exp(-0.3\phi_t)$

Strain rate sensitivity
$m(T, \phi_t) = 1/[m_0(T)(1 - m_\phi(T, \phi_t))]]$
with $m_0(T) = 77.68 M_{0T} + 4.11(1 - M_{0T}(T))$
  where $M_{0T}(T) = 1/[1 + \exp(10.2(T/692 - 1))]$
and $m_\phi(T, \phi_t) = 0.46\Phi(\phi_t)/[1 + \exp(14.49(T/870 - 1))]$

Strength
$K(T, \phi_t, \xi) = K_0(T)(1 + K_\phi(T, \phi_t, \xi))$
with $K_0(T) = (1.409 \times 10^9 - 1.1558 \times 10^6 T)K_{0T}(T) + 4.05 \times 10^7(1 - K_{0T}(T))$
  where $K_{0T}(T) = 1/[1 + \exp(6.62(T/1007 - 1))]$
and $K_\phi(T, \phi_t, \xi) = 0.42(1 - 6.44 \times 10^{-2}\phi_t\xi)\Phi(\phi_t)/[1 + \exp(19(T/768 - 1))]$

Strain hardening
$L(p, T, \phi_t) = (p + 1 \times 10^{-4})^{n_0(T,\phi_t)} \exp(-\alpha_n(T)p) + (p + 1 \times 10^{-4})^{n_\infty(T,\phi_t)}(1 - \exp(-\alpha_n(T)p))$
with $n_0(T, \phi_t) = n_{00}(T)(1 - n_{0\phi}(T, \phi_t))$
  with $n_{00}(T) = 7.9 \times 10^{-2} N_{00T}(T) + 3 \times 10^{-2}(1 - N_{00T}(T))$
    where $N_{00T}(T) = 1/[1 + \exp(4(T/620 - 1))]$
  and $n_{0\phi}(T, \phi_t) = 0.24\Phi(\phi_t)/[1 + \exp(7(T/630 - 1))]$
and $n_\infty(T, \phi_t) = n_{\infty 0}(T)(1 - n_{\infty\phi}(T, \phi_t))$
  with $n_{\infty 0}(T) = 5 \times 10^{-2} N_{\infty 0T}(T) + 5.6 \times 10^{-3}(1 - N_{\infty 0T}(T))$
    where $N_{\infty 0T}(T) = 1/[1 + \exp(5(T/590 - 1))]$
  and $n_{\infty\phi}(T, \phi_t) = 0.63\Phi(\phi_t)/[1 + \exp(7(T/630 - 1))]$
and $\alpha_n(T) = 40.45 \exp(2.03 \times 10^{-3} T)$

Anisotropy
$H_{rr}(T, \phi_t) = 0.485 + 9.5 \times 10^{-2}(1 - \Phi(\phi_t))/[1 + \exp(12(T/740 - 1))] + 0.32\Phi(\phi_t)/[1 + \exp(10(T/660 - 1))]$
$H_{zz}(T, \phi_t) = 0.52 + (-0.23 + 4 \times 10^{-4} T)(1 - \Phi(\phi_t))/[1 + \exp(15(T/550 - 1))] - 0.16\Phi(\phi_t)/[1 + \exp(20(T/920 - 1))]$

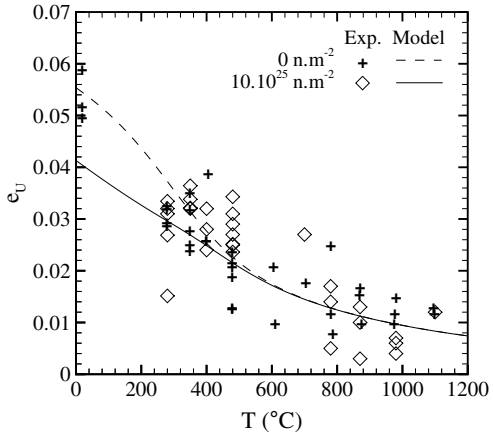

Fig. 8. Variation of the uniform plastic strain as a function of temperature for AT tests performed on the non-irradiated material and the irradiated material for 5 cycles (no strain rate and irradiation conditions effect).

3.3. Results and discussion

Fig. 2 compares experimental and simulated evolutions of S_U as a function of temperature for AT tests carried out under different strain rates on the non-irradiated material and the material irradiated for 5 cycles. The good agreement reveals the ability of the model to reproduce the influences of temperature, fluence and strain rate on the flow stress. Moreover, as depicted in Fig. 3, the model accurately captures the effects of irradiation conditions on material strength. Furthermore, the temperature, irradiation and plastic strain dependent strain hardening behavior of the material (Figs. 4 and 5), including uniform elongation (Fig 8), is correctly predicted by the model. Note in particular that the proposed formulation for the strain hardening coefficient, L, provides a better description of both plastic strain dependent strain hardening and uniform elongation than the classical power law type equation (replacing L by $p^{\bar{n}}$ in Eq. (8)) that includes only one average strain hardening parameter $\bar{n}$ and for which $\epsilon_U = \bar{n}$ under uniaxial tension (in accordance with the Considère's plastic instability criterion). Besides, plastic anisotropy is fairly well reproduced (Figs. 7, 9). Hence, the model provides a reasonable description of the material mechanical behavior within the studied domain, *i.e.* for temperatures from 20 °C up to 1100 °C, strain rates between 3×10^{-4} s^{-1} and 5 s^{-1} and fast neutron fluences from 0 nm^{-2} up to 10×10^{25} nm^{-2}.

The average value over the whole identification database of the relative error $|(y_{exp} - y_{sim})/y_{exp}|$ between experimental quantities (yield and flow stresses and uniform plastic strains), y_{exp}, and the corresponding simulated values, y_{sim}, is equal to about 8% on yield and flow stresses and 62% on uniform elongations, which is satisfactory compared to the experimental scatter (Figs. 2, 4, 8 and 9). Nevertheless, prediction capability of the model is expected to decrease with increasing temperature. Indeed, description of plastic anisotropy in particular is approximative for the upper part of the temperature range, due to the lake of data pertaining to HT tests and IP tests, especially over 600 °C for the irradiated material.

4. Example of FEA application

4.1. Introduction

The proposed model has been implemented into the finite element code Cast3M developed at CEA (http://www-cast3m.cea.fr/cast3m/index.jsp). Due to the geometry of the tubes, designs of the specimens used to measure fuel claddings axial and hoop tensile properties are not standardized. Finite element analysis (FEA) of the AT tests performed within the PROMETRA program showed that plastic strains and stresses are homogeneous within the gauge length of the specimens. Therefore, AT tests can be considered as uniaxial and axial tensile properties of fuel claddings can be derived straightforwardly from the measured load–displacement data using the standard procedure: plastic displacement is obtained by subtracting the effective elastic displacement from the mandrel total displacement (machine compliance and offset displacement are determined by standard means); engineering plastic strain is then calculated by dividing the plastic displacement by the initial calibrated gauge length and engineering stress is determined by dividing the load by the initial total cross-sectional area of the two gauges.

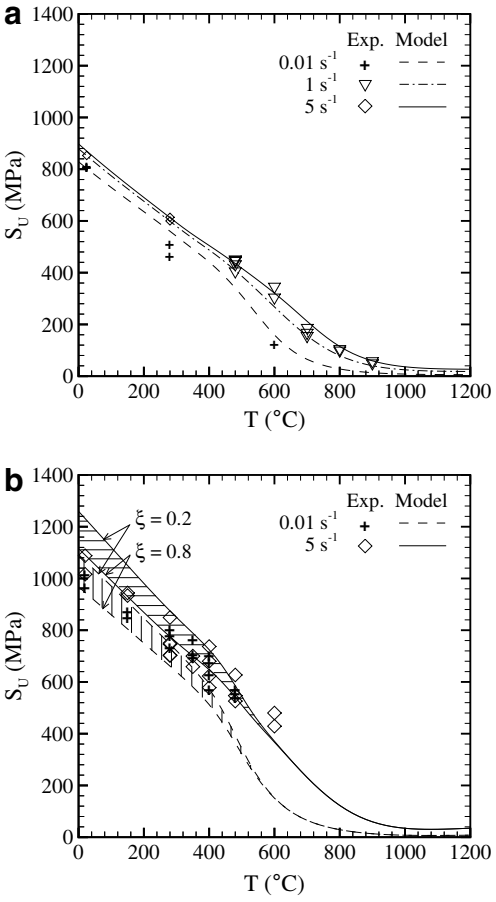

Fig. 9. Variation of the ultimate stress as a function of temperature and strain rate for HT tests performed (a) on the fresh material and (b) on the material irradiated for 5 cycles (fluence around 10×10^{25} nm^{-2}).

As specified in Section 2, interpretation of the ring HT tests performed within the PROMETRA program for evaluating the properties of the cladding material in the hoop direction is less obvious, because of structural effects that occur during the experiments (bending, friction, etc.). Due to the small size of the specimen and to the relative ease of the test achievement (suitable for a use in hot cells), the correct interpretation of the ring tensile test is an important issue for the study of the mechanical behavior of irradiated cladding materials. For this, FEA investigations are necessary to provide a further understanding of the test. An inverse method, combining FEA and tests results, was previously proposed to derive hoop stress–plastic strain properties from raw HT tests data [9,10]. Nevertheless, in the FEA of those studies, plastic anisotropy and viscosity of the material as well as friction between the

sides of the mandrels and the sample gauges were not hitherto taken into account. Here, a more precise simulation of the tests was developed in order to examine the consequences of structural artefacts and check if the direct conversion of the raw load–displacement data to stress–plastic strain properties results in significant discrepancies compared to the intrinsic mechanical properties of the material.

4.2. Geometry and finite element modeling

The ring specimen used within PROMETRA consists of a 5 mm large small ring with two gauges of 3 mm length and 2 mm width (Fig. 1). The sample is placed around two half-cylinder inserts attached to the cross-heads and pulled apart inside the ring. No lubrification is used between the mandrels and the specimen. The mandrels are designed to have a gap of about 30 μm between their sides and the sample gauges in order to minimize the combined effects of bending and friction. Load and cross-head displacement are measured during the experiments.

Brick elements with quadratic interpolation (20 nodes, 27 Gauss points) are used for the calculations, based on a large displacement and large strain formulation. According to the symmetries, only 1/8 of the system is considered. Standard boundary conditions are applied and a contact area involving sliding with friction is defined between the inner surface of the ring specimen and the outer surface of the die inserts. Friction is modeled by the classical Coulomb's friction law (friction coefficient, μ). An initial gap, g, is introduced between the sides of the mandrels and the specimen gauges. The cross-head displacement is applied on the tangential direction of the sample gauge section. The set of constitutive equations proposed in the present paper is used to describe the mechanical behavior of the cladding specimens.

4.3. Results and discussion

Due to bending and friction, plastic strain and stress fields are not homogeneous within the calibrated parts of the ring sample: plastic strains are concentrated in the middle of the calibrated region and strain and stress gradients are observed through the sample thickness (Fig. 10). Note that local deformations of the specimen are influenced by plastic anisotropy of the material. The influence on structural artefacts of temperature, strain rate, fluence, initial gap and friction coefficient between the ring specimen and the mandrels have been analyzed. The methodology consists in comparing the intrinsic hoop stress–plastic strain properties (response of an elementary representative volume undergoing a pure hoop tensile loading) predicted by the set of constitutive equations proposed in the present paper and those deduced from three-dimensional FEA of the HT tests. The conversion of load–displacement data calculated by FEA into engineering stress–plastic strain relationship has been performed by applying the standard procedure stated above, *i.e.* using the initial cross-sectional area and the initial calibrated gauge length. Nevertheless, a more local estimation of plastic strain can be obtained from FEA by computing the area-averaged plastic strain at the center of the specimen gauges. Then, an effective gauge length can be defined so that the ratio between the plastic displacement and this length corresponds to the aforementioned area-averaged plastic strain. Differences between intrinsic and FEA-calculated plastic strain, stress and uniform elongation measurements are discussed below.

4.3.1. Stress–plastic strain relationship

Structural artefacts can be quantified by the relative difference between FEA and intrinsic flow stress for a given global strain (Fig. 11). The term global refers to quantities deduced from the measured load–displacement data. Artefacts are shown to be significant both in the elastic regime and at the beginning of global plasticity. For all testing conditions, the yield stress deduced from FEA is 10–20% lower than the intrinsic stress at the onset of plasticity, since the gauge section is submitted to a combination of tensile and bending loads. Yet, as the bending contribution rapidly decreases during deformation, this underestimation does not exceed 10% on S_U whatever the testing conditions.

4.3.2. Plastic strain

The difference between intrinsic and FEA-obtained stress–plastic strain data may be partially due to the fact that the 3 mm calibrated length (which is commonly used as the gauge length to interpret test data) does not rigorously pertain to the effective gauge length. Indeed, as illustrated in Fig. 12, the instantaneous effective gauge length determined by FEA varies during loading, in particular for low global plastic deformations (lower than about 0.005). As a consequence of bending, whereas no plasticity is expected at the beginning of the test according to the measured global response, plastic deformation occurs locally within the gauge

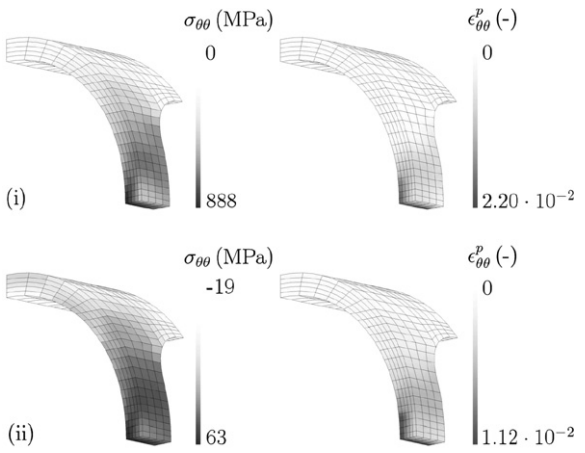

Fig. 10. Stress and plastic strain fields in the hoop direction calculated at a global plastic strain of 0.01 for HT tests performed at a displacement rate of 15 mm s^{-1} at (i) 350 °C and (ii) 900 °C with $\mu = 0.4$ and $g = 0.3$ μm on the material irradiated for 5 cycles (with $\xi = 0.5$).

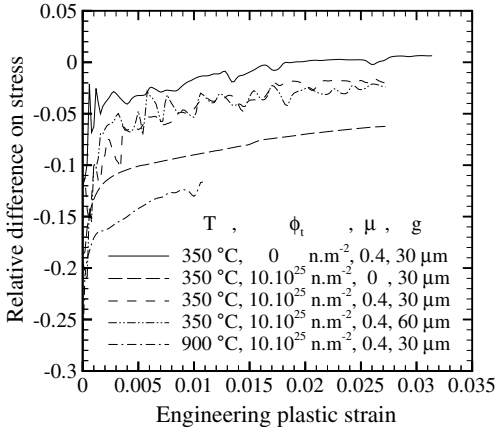

Fig. 11. Calculated variation as a function of the global plastic strain up to the intrinsic uniform elongation of the relative difference between the FEA-obtained (using the standard procedure) and the intrinsic engineering stress levels for HT tests performed at a displacement rate of 15 mm s^{-1} under various conditions with $\xi = 0.5$ for the irradiated material.

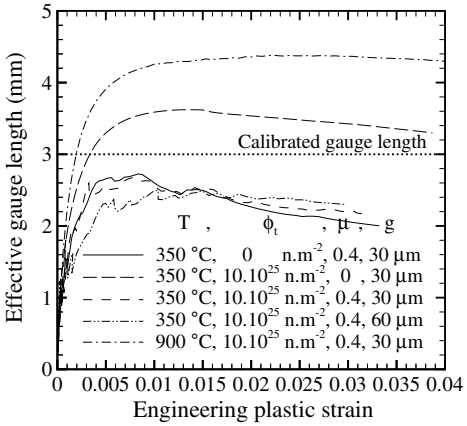

Fig. 12. Calculated variation of the effective gauge length as a function of the global plastic strain up to uniform elongation for HT tests performed at a displacement rate of 15 mm s^{-1} under various conditions with $\xi = 0.5$ for the irradiated material.

section. Furthermore, while the effective gauge length decreases with increasing friction coefficient and initial gap, it increases with increasing test temperature. Indeed, the strain rate sensitivity of the material flow strength significantly increases with increasing temperature between about 400 °C and 800 °C. Therefore, as a high strain rate sensitivity tends to stabilize strain localization within the gauge parts, specimen deformation is more diffuse at higher temperatures. For example, at 350 °C for $\mu = 0.4$ the effective gauge length is about 2–2.5 mm for global plastic strain greater than 0.005, while it is approximately 4–4.5 mm at 900 °C. As a consequence, by using the calibrated length of 3 mm, plastic strain is underestimated by up to 50% at 350 °C and overestimated by up to 30% at 900 °C.

4.3.3. Stress

The underestimation of stress values is amplified with increasing fluence and more significantly with increasing temperature. Indeed, discrepancy between the actual strain rate within the gauge section and the expected strain rate (imposed displacement rate divided by the calibrated gauge length) is logically of the same order of magnitude as for plastic strain (approximately a 50% underestimation at 350 °C and a 30% overestimation at 900 °C). This may importantly influence the specimen reponse, in particular at high temperatures for which the flow stress strongly depends on strain rate. For example, at 900 °C, according to the constitutive equation proposed in the present paper, the ultimate stress in the hoop direction decreases by about 9% when the strain rate is 3.5 s^{-1} ($= 70\% \cdot 5$ s^{-1}) instead of the expected 5 s^{-1}. On the other hand, the difference between the intrinsic stress level and that deduced from FEA decreases with increasing the friction coefficient between the ring specimen and the die inserts. A quite good correlation is obtained for a friction coefficient of 0.4 (Fig. 11), which appears to be a realistic value considering the surface roughness of the irradiated samples and the absence of lubrification between the mandrels and the specimen.

4.3.4. Uniform elongation

In conformity with these observations, necking is substantially influenced by testing conditions: strain localization is enhanced with increasing friction coefficient and initial gap and delayed with increasing temperature. For example, for the material irradiated for 5 cycles tested at 350 °C, the uniform elongation is overestimated by about 40% for $\mu = 0$ and $g = 30$ μm, 20% for $\mu = 0.4$ and $g = 30$ μm and 40% for $\mu = 0.4$ and $g = 0$ μm. At 900 °C for $\mu = 0.4$ and $g = 0.3$ μm, the global uniform plastic strain is more than twice greater than the intrinsic one, probably as a consequence of the high strain rate sensitivity of the material that confers to the ring specimen a high resistance to necking. These results justify that uniform elongation measured during HT tests were not taken into account in the identification procedure described in Section 2.

According to this analysis, structural artefacts become relatively low for global hoop plastic strain levels greater than about 0.005. Then, one can consider that the stress–plastic strain properties directly evaluated from the raw load–displacement data are satisfactorily accurate in that range. However, the use of the effective gauge length deduced from FEA for each testing condition instead of the calibrated length should significantly improve the predictions. Besides, a better knowledge of the value of the friction coefficient between the ring specimen and the mandrels is essential for further understanding of the test. An experimental evaluation of this coefficient is currently in progress. The iterative method previously mentioned can then be used to refine the assessment of the hoop mechanical properties if necessary.

5. Conclusions

The anisotropic viscoplastic mechanical behavior of fresh and irradiated CWSR Zircaloy-4 fuel claddings has been analyzed on the basis of axial tensile, hoop tensile and closed-end internal pressurization tests results mainly extracted from the PROMETRA database, appropriate in the field of RIA studies. In particular, the effects of temperature (from 20 °C up to 1100 °C), strain rate (from 3×10^{-4} s^{-1} up to 5 s^{-1}), fluence (from 0 nm^{-2} up to 10×10^{25} nm^{-2}) and irradiation conditions (irradiation temperature or, in the absence thereof, axial position of the sample along the fuel cladding) on the inelastic properties of the material have been investigated. A phenomenological model, based on a unified multiplicative viscoplastic formulation, was developed in order to reproduce these material features. Plastic anisotropy is introduced using a temperature and irradiation dependent Hill's yield criterion. Then, the model ability to simulate the whole experimental database mentioned above has been demonstrated. Finally, the efficiency of the present model for finite element applications has been illustrated. In particular, the hoop tensile tests performed within the PROMETRA program have been analyzed and validity of the stress–plastic strain properties deduced from the tests was discussed.

The model proposed in the present paper only describes the mechanical behavior of the material and does not reproduce its fracture. In order to provide a better understanding of the failure mechanisms of fuel claddings during RIAs, with the aim of predicting their survivability, a Gurson–Tvergaard–Needleman (GTN) type model [32–34], coupling the deformation model described in the present paper with damage, is conjointly developed. In particular, since hydride embrittlement has been identified as one of the main limiting phenomenon to burnup increase [2], the analysis of the influence of hydride precipitates on the ductile fracture (*i.e.* void nucleation, growth and coalescence) of cladding tubes is envisioned. Determination and identification of the model parameters will be performed by combination of numerical simulations and reliable out-of-pile experiments developed elsewhere carried out under RIA loading conditions [35].

Acknowledgements

The authors would like to thank all people who contributed to the realization of the PROMETRA program. The financial and technical support from Institut de Radioprotection et de Sûreté Nucléaire and Electricité de France is also acknowledged.

References

[1] E. Federici, F. Lamare, V. Bessiron, J. Papin, in: Technical Committee Meeting on Fuel Behaviour Under Transient and LOCA Conditions, IAEA-TECDOC-1320, Halden, Norway, 2001, p. 88.
[2] J. Papin, B. Cazalis, J. Frizonnet, J. Desquines, F. Lemoine, V. Georgenthum, F. Lamare, M. Petit, Nucl. Technol. 157 (3) (2007) 230.
[3] P. Delobelle, P. Robinet, P. Geyer, P. Bouffioux, J. Nucl. Mater. 238 (1996) 135.
[4] I. Schäffler, P. Geyer, P. Bouffioux, P. Delobelle, J. Eng. Mater. Technol. 122 (2000) 168.
[5] L. Jernkvist, in: 15th International Conference on Structural Mechanics in Reactor Technology, No. C04/3, Seoul, Korea, 1999, p. II-477.
[6] F. Onimus, J. Béchade, C. Prioul, P. Pilvin, I. Monnet, S. Doriot, B. Verhaeghe, D. Gilbon, L. Robert, L. Legras, J. Mardon, in: 14th International Symposium on Zirconium in the Nuclear Industry, ASTM STP 1467, vol. 2, Stockholm, Sweden, 2004, p. 53.
[7] S. Leclercq, G. Rousselier, G. Cailletaud, Mech. Mater. 39 (2007) 458.
[8] P. Geyer, Comportement elasto-viscoplastique de tubes en Zircaloy-4: approche expTrimentale et modTlisation micromTcanique, PhD Thesis, Ecole des Mines de Paris, France, 1999.
[9] M. Balourdet, C. Bernaudat, V. Basini, N. Hourdequin, in: 15th International Conference on Structural Mechanics in Reactor Technology, No. C04/4, Seoul, Korea, 1999, p. II-485.
[10] P. Yvon, C. Sainte Catherine, C. Duguay, N. Hourdequin, in: Technical Committee Meeting on Fuel Behaviour Under Transient and LOCA Conditions, IAEA-TECDOC-1320, Halden, Norway, 2001, p. 111.
[11] J. Desquines, B. Cazalis, C. Bernaudat, C. Poussard, X. Averty, P. Yvon, in: 14th International Symposium on Zirconium in the Nuclear Industry, ASTM STP 1467, vol. 2, Stockholm, Sweden, 2004.
[12] B. Cazalis, J. Desquines, C. Poussard, M. Petit, Y. Monerie, C. Bernaudat, P. Yvon, X. Averty, Nucl. Technol. 157 (2007) 215.
[13] S. Arséne, J. Bai, J. Test. Eval. 26 (1) (1998) 26.
[14] T. Sugiyama, N. Nagase, T. Fuketa, in: International Topical Meeting on Light Water Reactor Fuel Performance, Kyoto, Japan, 2005, p. 912.
[15] R. Daum, S. Majumdar, H. Tsai, T. Bray, D. Koss, A. Motta, M. Billone, in: Fourth International Symposium on Small Specimen Test Techniques, ASTM STP 1418, 2002, p. 195.
[16] M. Billone, The Mechanical Properties Experts Group Update on Round Robin Test Results, February 2001.
[17] R. Limon, J. Béchade, S. Lehmann, R. Maury, A. Soniak, J. Mardon, in: Journées d'Etudes Propriétés – Microstructure, Le Zirconium, Saclay, France, 1995, p. 133.
[18] K. Elbachiri, J. Crepin, T. Bretheau, V. Rebeyrolle, in: 16éme Congrés Frantais de Mécanique, Nice, France, 2003.
[19] D. Northwood, R. Gilbert, L. Bahen, P. Kelly, R. Blake, A. Jostsons, D. Faulkner, W. Bell, R. Adamson, J. Nucl. Mater. 79 (1979) 379.
[20] C. Regnard, B. Verhaeghe, F. Lefebvre-Joud, C. Lemaignan, in: 13th International Symposium on Zirconium in the Nuclear Industry, ASTM STP 1423, Annecy, France, 2001, p. 384.
[21] T. Tomimura, T. Yasuda, M. Nakatsuka, J. Nucl. Mater. 238 (1996) 169.
[22] N. Christodoulou, S. St Lawrence, C. Chow, in: 19th International Conference on Structural Mechanics in Reactor Technology, No. D03/1, Toronto, Canada, 2007.
[23] T. Link, T. Koss, A. Motta, Nucl. Eng. Des. 186 (1998) 379.
[24] F. Onimus, J. Béchade, D. Gilbon, P. Pilvin, J. Nucl. Mater. 358 (2006) 176.
[25] K. Lee, S. Kim, K. Kim, S. Hong, J. Nucl. Mater. 295 (2001) 21.
[26] K. Murty, I. Charit, Prog. Nucl. Energy 48 (2006) 325.
[27] E. Tenckhoff, in: 14th International Symposium on Zirconium in the Nuclear Industry, ASTM STP 1467, vol. 2, Stockholm, Sweden, 2004, p. 25.
[28] M. Nakatsuka, M. Nagai, J. Nucl. Sci. Technol. 24 (1987) 32.
[29] S. Yagnik, A. Hermann, R. Kuo, in: 14th International Symposium on Zirconium in the Nuclear Industry, ASTM STP 1467, vol. 2, Stockholm, Sweden, 2004, p. 604.
[30] S. Mahmood, W. Daugherty, K. Murty, in: 10th International Conference on Structural Mechanics in Reactor Technology, No. C02/4, Anaheim, California, 1989, p. 59.
[31] R. Hill, The Mathematical Theory of Plasticity, Clarendon, Oxford, 1950.
[32] A. Gurson, J. Eng. Mater. Technol. 99 (1977) 2.
[33] V. Tvergaard, A. Needleman, Acta Metall. 32 (1984) 157.
[34] M. Grange, J. Besson, E. Andrieu, Int. J. Fract. 105 (2000) 273.
[35] M. Le Saux, C. Poussard, X. Averty, C. Sainte Catherine, J. Besson, in: International Topical Meeting on Light Water Reactor Fuel Performance, San Francisco, California, 2007, p. 526.